SCIENTIFIC REPORTS

OPEN

SUBJECT AREAS:
QUANTUM OPTICS
MICRO-OPTICS
QUANTUM INFORMATION
QUBITS

Received
7 November 2013

Accepted
29 January 2014

Published
18 February 2014

Correspondence and requests for materials should be addressed to A.S. (alexander.szameit@uni-jena.de)

Arbitrary photonic wave plate operations on chip: Realizing Hadamard, Pauli-X, and rotation gates for polarisation qubits

René Heilmann, Markus Gräfe, Stefan Nolte & Alexander Szameit

Institute of Applied Physics, Abbe Center of Photonics, Friedrich-Schiller-Universität Jena, Max-Wien-Platz 1, 07743 Jena, Germany.

Chip-based photonic quantum computing is an emerging technology that promises much speedup over conventional computers at small integration volumes. Particular interest is thereby given to polarisation-encoded photonic qubits, and many protocols have been developed for this encoding. However, arbitrary wave plate operation on chip are not available so far, preventing from the implementation of integrated universal quantum computing algorithms. In our work we close this gap and present Hadamard, Pauli-X, and rotation gates of high fidelity for photonic polarisation qubits on chip by employing a reorientation of the optical axis of birefringent waveguides. The optical axis of the birefringent waveguide is rotated due to the impact of an artificial stress field created by an additional modification close to the waveguide. By adjusting this length of the defect along the waveguide, the retardation between ordinary and extraordinary field components is precisely tunable including half-wave plate and quarter-wave plate operations. Our approach demonstrates the full range control of orientation and strength of the induced birefringence and thus allows arbitrary wave plate operations without affecting the degree of polarisation or introducing additional losses to the waveguides. The implemented gates are tested with classical and quantum light.

Quantum information science addresses various fundamental questions on how to harness quantum mechanical phenomena for storing, processing and transmitting information[1]. Therefore, quantum information is both fundamental science and a progenitor for new technologies[2]. One of the most intricate future technology is the quantum computer which promises exponentially faster operation for particular tasks such as factorising, searching databases and simulating important quantum systems[1]. Along these lines a number of physical systems for the development of well-performing quantum computers have been investigated, such as ultracold atoms and trapped ions, spin chains, cavity quantum electro dynamics, superconductors, and liquid state NMR[3–8]. In addition, those systems involving photonic quantum states seem likely to play a central role as light is a logical choice when dealing with quantum communication, metrology and lithography. Moreover, photons are in general more immune to decoherence than other quanta.

However, a downside of photonic quantum architectures is the complex setting, at least when using bulk optical systems: Building more complex networks of logic gates encounters severe size and stability limitations. A promising approach to miniaturising and scaling optical quantum circuits is to use on-chip integrated photonic waveguides[2], which show strong improvements in performance due to high stability and low noise – crucial aspects for high-fidelity classical and quantum interference.

In recent years various breakthroughs were presented, in which the integration of quantum circuits using optical waveguides played an important role. The first landmark was the implementation of a photonic quantum gate on a chip, employing silica-on-silicon waveguides[9]. Using this approach it was shown that it is possible to realise one of the most important quantum gates - the C-NOT gate - on a chip, for path-entangled photons. This first seminal work was followed by various follow-up publications, in which the potential of integrated quantum optics was explored: Integration of controlled phase shifters in integrated interferometers has been used to manipulate entangled states of up to four photons and to demonstrate on-chip quantum metrology[10]. A compiled version of Shor's quantum factoring algorithm was performed on chip consisting of several one- and two-qubit gates[11]. Moreover, an on-chip waveguide architecture was employed for the demonstration of continuous-time quantum random walks of path-entangled photons[12]. And only recently even a boson sampling computation was executed (besides using bulk optics[13]) on a photonic chip[14–16].

Importantly, photons exhibit polarisation, a two-level degree of freedom that carries numerous benefits when encoding qubits[17]. Using polarisation entanglement is highly beneficial as various entangled-photon sources are available[18], and many quantum information protocols and experiments have been developed for this encoding[19–22]. An arbitrary polarisation transformation, which means to have the ability of preparing a single qubit in any desired state, was shown for telecom wavelength using the electro-optical effect in titanium-diffused lithium niobate waveguides[23,24]. Pushing towards the visible regime it turned out that waveguide architectures fabricated using the femtosecond laser-writing technique[25] are particularly useful for polarisation-encoded on-chip quantum optics due to the low birefringence and, consequently, low decoherence[26]. This sophisticated fabrication approach allowed the realisation of C-NOT gates with polarisation encoding[27]. Laser-written waveguides are also an exceptional platform for implementing discrete-time[28] and continuous-time quantum random walks[29]. Moreover, three-dimensional geometries are feasible with such architectures[30].

In our work, we go the next consequent step in the development of laser-written integrated quantum circuits and present *photonic Hadamard gates, Pauli-X gates, and rotation gates on chip*. In particular the Hadamard gate is one of the three universal quantum gates (besides the C-NOT gate and the $\pi/8$-gate) which, according to the quantum circuit model, represent a set of building blocks that efficiently approximate any conceivable quantum operation if arranged in a given finite sequence[1]. Therefore, our results constitute a crucial leap towards polarisation-entangled quantum computing on chip.

Results

For the fabrication of the integrated quantum gates as well as the general wave plates we employ the femtosecond laser-writing technique[25]. Only recently it was shown that the birefringence in a laser written waveguide can be precisely tuned by employing particular line defects close to the waveguide[31]. However, in this work the optical axis of the birefringent waveguides was always fixed either along the vertical or the horizontal direction, preventing an actual Hadamard operation. We generalise this approach in order to freely choose the orientation of the waveguide's optical axis, whereas the waveguides themselves remain in their original orientation. With our approach we are able to implement arbitrary desired polarisation transformations, including the Hadamard operation.

Importantly, laser-written waveguides are surrounded by an extended stress field that is created during the writing process[32]. So far, this stress field has been used to alter the strength of the birefringence of adjacent waveguides[31]; however, there was no impact on its vectorial character.

Our experimental analysis of this phenomenon delivers the surprising result that, when an additional waveguide is prone to such a stress field, an artificial birefringence is induced in this guide, which results in a reorientation of the optical axis as a function of the relative position of the two guides. As the relative position (in distance and angle) can be tuned with high precision, strong tilting of the birefringent axis can be implemented at will, allowing arbitrary desired wave plate operations on the light that propagates in the waveguide exposed to the stress field. A sketch of this effect is shown in Fig. 1(a). To prevent the system from coupling light to the defect, the defect is written slightly above the destruction threshold. The main advantage of our approach is that the original waveguide shape remains unchanged irrespective of the optical axis' orientation that causes the wave plate operation. Hence, there is no additional friction of the propagating light caused by the artificial birefringence The additional losses in presence of the defect are <0.01 dB/cm.

In order to test the functionality of our approach, we first perform a series of classical measurements using free space cw laser light at $\lambda = 815$ nm (Spectra Physics Tsunami) that is launched into the integrated wave plate using a 10× objective (NA = 0.25) and

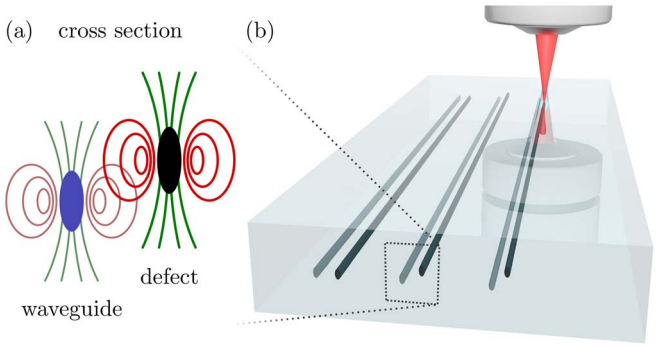

Figure 1 | Settings. (a) Idealised schematic showing the cross section of the waveguide arrangement where additional stress fields induce a reorientation of the waveguide's optical axis. (b) Sketch of the writing setting, with which the quantum gates are fabricated (here for 3 different orientations of the defect relatively to the waveguide). Higher pulse energies and lower writing velocity for the defects causes their missing light guiding properties and, hence, prevent loss due to coupling.

projected onto a power meter using a 4× objective (NA = 0.10). In our experimental analysis the distance between the waveguide and the defect is $r = 20$ µm, such that the introduced stress field is large enough to change the optical axis of the target waveguide without disturbing its mode profile. As a benefit it turned out that only a defect on one side is necessary to obtain the desired effect while the degree of polarisation is still retained ($>1000:1$). We characterise the strength of the birefringence as well as the orientation of the optical axis following a method proposed by Yang et al.[33]. Two crossed polarisers encircle the optical chip and are rotated simultaneously over the desired range. The signal on the power meter drops to zero only if the polarisers are orientated along the fast or slow axis of the investigated wave plate. Further rotating the polarisers by 45° the maximum power is transmitted and discloses the strength of the birefringence. Detailed information can be found in the method section.

We extract a birefringence in the waveguide that is $\Delta n = 0.65 \ldots 1.32 \times 10^{-5}$, depending of the azimuthal angle of the defect caused by the resulting overlap of the stress fields. The orientation of the optical axis as a monotonous function of the azimuthal angle θ of the defect is plotted in Fig. 2(a). For increasing θ also the tilt of the waveguide's optical axis α increases (in a nonlinear fashion) and reaches a maximum of $\alpha_{\max} = 90°$ for $\theta = 90°$. In order to understand our experimental data, we developed a simple heuristic model. As the birefringence in the waveguide is increased by approximately one order of magnitude in the presence of a defect, we consider only the defect's stress fields, represented by their centroids on either sides of the defect with coordinates (r_i, θ_i) with respect to the waveguide. Assuming that the impact s_i of such a stress field i on the optical axis decreases exponentially with growing distances by the decay rate ρ, we obtain for our data the fit function

$$\alpha(\theta) = \frac{\sum_{i=1,2} \theta_i s_i}{\sum_{i=1,2} s_i} = \frac{\sum_{i=1,2} \arctan\left(\frac{r\sin\theta + d_{\mathrm{vert}}}{r\cos\theta + (-1)^i d_{\mathrm{hor}}}\right) e^{-r_i/\rho}}{\sum_{i=1,2} e^{-r_i/\rho}}, \qquad (1)$$

with $r_i = \sqrt{(r\sin\theta + d_{\mathrm{vert}})^2 + \left(r\cos\theta + (-1)^i d_{\mathrm{hor}}\right)^2}$ and $d_{\mathrm{hor,vert}}$ as horizontal or vertical deposition, respectively, of the stress fields' centroids compared to the centre of the defect. The best fit shows $\rho = 20(3)$, µm $d_{\mathrm{hor}} = 7.95(10)$ µm, and $d_{\mathrm{vert}} = -4.2(6)$ µm, suggesting that the centroids tend to lie below the envisaged level, which is caused by an elongated shape of the defect leading to an offset of $\theta_0 = 11.9°$ for zero-crossing. For smaller angles the experimental data deviate from the predicted line leading to a tilt of the wave-

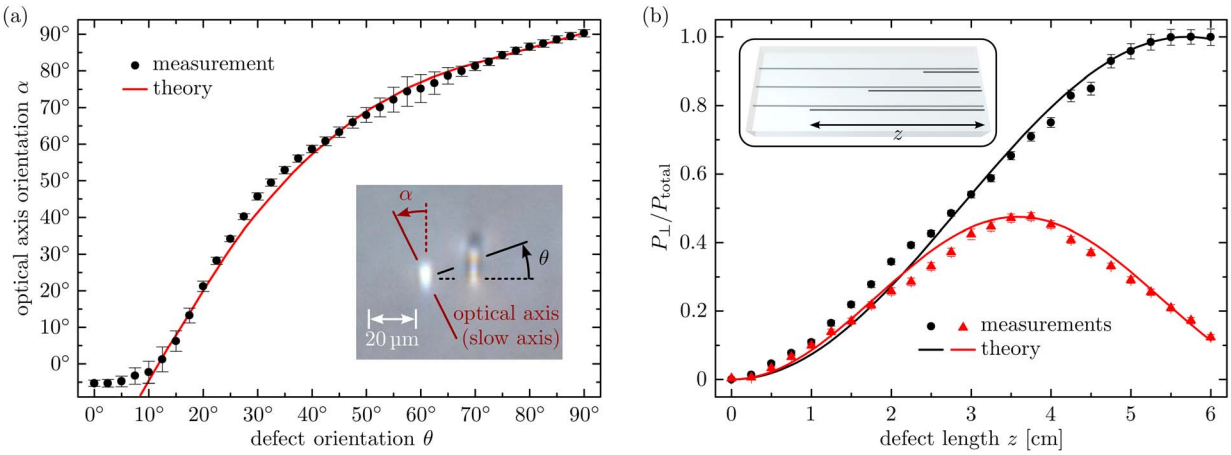

Figure 2 | Measured wave plate operations. (a) Experimental data and best fit model of the reorientation of the optical axis as a function of the azimuthal position of the defect. Larger error bars result from near λ operation of the integrated wave plate. (b) Intensity ratio $P_\perp/P_{\text{total}}$ between the power of the perpendicularly polarised light (H or V polarisation) and the total power as a function of the interaction length between defect and waveguide (assumed to be proportional to $\Delta\varphi$). The angle of the optical axis is fixed to $\alpha = 45^\circ$ (black dots) or $\alpha = 22.5^\circ$ (red triangles) and $P_\perp/P_{\text{total}}$ should follow $(\sin(2\alpha)\,\sin(\Delta\varphi/2))^2$.

guide's optical axis by $\alpha = -6^\circ$ at $\theta = 0^\circ$. This is due to the sequenced writing of the waveguide followed by the defect that has to be written in or through a yet present glass modification, which affects most notably the stress field on the left side of the defect. Hence, both stress fields will lie in different depths and the assumed symmetry, $d_{\text{vert},1} = d_{\text{vert},2}$, is broken.

Clearly, with this tuning degree of freedom we can produce arbitrary wave plate operations, including the Hadamard gate, the Pauli-X gate, and a rotation gate. First, the realisation of those gates depends on the correct orientation of the optical axis ($\alpha = 22.5^\circ$ or 45.0°) which is tuned by the position of the defect given by the angle θ. Second, it depends on the defect length z, since for increasing interaction length the phase delay $\Delta\varphi$ between the slow and the fast axis increases as well (see Fig. 2(b)). Table I outlines the corresponding parameters for implementing the gates.

The fabricated Pauli-X and Hadamard gates are particularly interesting for quantum applications, as especially the latter is part of a simple set of universal quantum gates (besides the C-NOT gate and the $\pi/8$-gate). Hence, we experimentally demonstrate their functionalities also in the single photon regime. When a single photon in either horizontal $|H\rangle$ or vertical $|V\rangle$-polarisation representing the $|0\rangle$ or $|1\rangle$ state, respectively, enters a single qubit gate, the gate operation is generally described by the basis transformation

$$|\Psi\rangle = a|H\rangle + b|V\rangle = \begin{pmatrix} a \\ b \end{pmatrix} \rightarrow |\Psi_{\text{out}}\rangle = M|\Psi_{\text{in}}\rangle \qquad (2)$$

where M is a 2×2 matrix. In case of the Hadamard gate, the transformation matrix

$$M_{\text{Had}} = \frac{1}{\sqrt{2}} \begin{pmatrix} 1 & 1 \\ 1 & -1 \end{pmatrix} \qquad (3)$$

is applied, which transforms a photon in the $|H\rangle$ state into the (diagonal) $|D\rangle$ state

Table I | Gate parameters

gate	α	θ	$\Delta\varphi$	z
Hadamard	22.5°	20.5(2)°	π	3.6(1) cm
Pauli-X	45.0°	29.7(3)°	π	5.6(1) cm
rotation	45.0°	29.7(3)°	$\pi/2$	2.8(1) cm

Outline of the corresponding parameters for implementing the Hadamard, Pauli-X, and a rotation gate. Note, only the relative positioning angle of the defect θ and the defect length z are experimentally tuned.

$$|H\rangle \rightarrow |D\rangle = \frac{|H\rangle + |V\rangle}{\sqrt{2}} \qquad (4)$$

and a photon in the $|V\rangle$ state into the (anti-diagonal) $|A\rangle$ state

$$|V\rangle \rightarrow |A\rangle = \frac{|H\rangle - |V\rangle}{\sqrt{2}}. \qquad (5)$$

Discussion

The performance of the fabricated Hadamard gate is best reflected by its measured matrix that is shown in Fig. 3(a) and which depicts the response of the system as a function of the input state. It is clearly seen that indeed $|H\rangle$ and $|V\rangle$ input states are successfully transformed into $|D\rangle$ and $|A\rangle$ states, respectively. From our measurement data, we retrieve the experimental transformation matrix in the $|H\rangle$, $|V\rangle$ basis for our Hadamard gate

$$M_{\text{Had}}^{\text{exp}} = \frac{1}{\sqrt{2}} \begin{pmatrix} 1.014 - i0.012 & 0.996 \\ 0.986 & -1.003 - i0.025 \end{pmatrix}, \qquad (6)$$

which is very close to the ideal (theoretical) Hadamard operation with a fidelity $\left(\mathcal{F}^{|\Psi\rangle} = \left|\langle\Psi|M_{\text{ideal}}^{*} M_{\text{exp}}|\Psi\rangle\right|^2\right)^1$ of $\mathcal{F}_{\text{Had}}^{|H\rangle,|V\rangle} = 0.999(5)$. The error of the matrix elements ranges from 0.010 to 0.016 and originates from the Poissonian statistics of the single photons and the precision of the adjusted measurement bases. From the modulus of the matrix elements we deduced the orientation of the optical axis to be $\alpha_{\text{Had}} = 22.3(4)^\circ$. The optimal value of $\alpha = 22.5^\circ$ describes a transformation, e.g., from $|H\rangle$ to $|D\rangle$, i.e., with equal coefficients for $|H\rangle$ and $|V\rangle$. The slight discrepancy suggests that $|H\rangle$ and $|V\rangle$ are not perfectly balanced. The non-zero imaginary part indicates deviations from a perfect half-wave plate operation, where $\Delta\varphi$ should reach exactly π (see Table I). Hence, depending on the portion of the imaginary part the resulting state suffers from left or right rotating components. The experimental gate shows an almost vanishing imaginary part resulting in an $\Delta\varphi_{\text{Had}} = 1.01(2)\pi$ fulfilling the desired condition.

The Pauli-X gate is defined by the basis transformation

$$M_{\text{PX}} = \begin{pmatrix} 0 & 1 \\ 1 & 0 \end{pmatrix}, \qquad (7)$$

i.e., it flips the $|H\rangle$ and $|V\rangle$ states: $|H\rangle \rightarrow |V\rangle$ and vice versa. The experimental Pauli-X matrix (see Fig. 3(b)) reads as follows

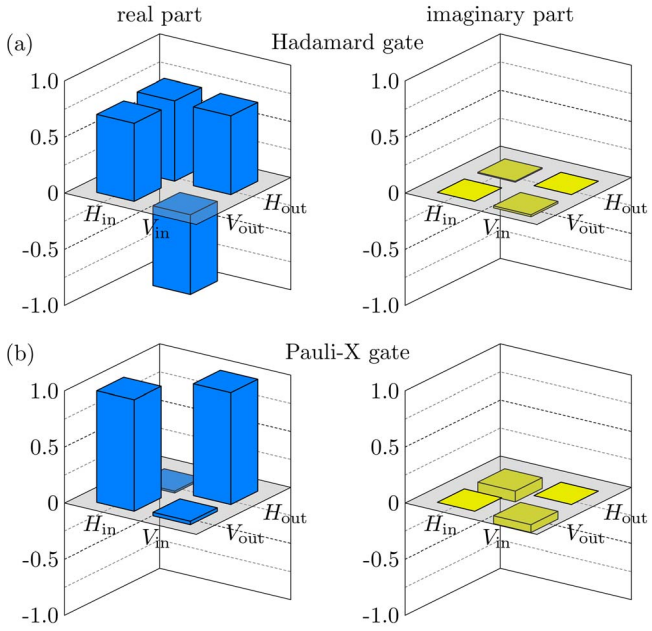

Figure 3 | Measured gate matrices. Real and imaginary part of the measured transformation matrices for the Hadamard operation (a) and the Pauli-X operation (b).

$$M_{PX}^{exp} = \begin{pmatrix} -0.017 - i0.096 & 0.997 \\ 0.995 & 0.031 - i0.070 \end{pmatrix} \quad (8)$$

and yields a fidelity of $\mathcal{F}_{PX}^{|H\rangle,|V\rangle} = 0.992(7)$. The extracted values of the wave plate operation are $\alpha_{PX} = 45.7(7)^\circ$ and $\Delta\varphi_{PX} = 1.05(2)\pi$, which confirms the first implementation of a polarisation swapping device on a chip.

In conclusion, we demonstrate a new approach to fabricate arbitrary wave plates in optical integrated devices using induced birefringence allowing precise control of the waveguide's optical axis orientation. Therewith, we successfully performed a Hadamard and a Pauli-X operation on both classical and quantum states of light, which constitutes a benchmark for a full manipulation of polarisation-encoded qubits on-chip. Our results disclose new scenarios for integrated quantum computation, quantum information processing, and quantum simulation, and possibly find application in standard photonic devices whenever integrated and finely controllable birefringent devices are of interest.

Methods

Direct waveguide writing. We write our waveguides into transparent fused silica wafers (Corning 7980 ArF Grade), using ultrashort laser pulses ($\tau \approx 150$ fs, $\lambda = 800$ nm) that are focused 250 μm below the sample surface using a 20× microscope objective (NA = 0.35). The defect that rotates the optical axis of the original waveguides is written with a higher pulse energy and lower writing velocity slightly above the destruction threshold, such that these defects do not guide light. However, their stress field induces a strong birefringence in the waveguide, with an orientation that is determined by the relative position of the defect with respect to the guide. For a sketch of the writing setting see Fig. 1(b); a microscope image of a written structure is shown in the inset of Fig. 2(a). The actual writing speed is 60 mm/min at a pulse energy of 200 nJ and a repetition rate of 100 kHz (Coherent Mira/Reg A). Such waveguides exhibit low propagation losses (<0.3 dB/cm) and almost vanishing birefringence ($\Delta n_{H,V} \approx 10^{-6}$). With a supported mode field diameter of 12 μm × 15 μm coupling losses of 3 dB are obtained with standard single mode fibres.

Determining orientation and strength of the birefringence. The birefringent properties of the individual waveguides are obtained by placing a polariser (Pol) at each side of the sample. The polariser after the quarter-wave plate (QWP) is used for preselecting the polarisation direction of the light beam at the input facet. The crossed polariser at the output is then used to analyse the transmitted light. From the positions of the transmission minima as a function of the polariser's rotation angle (see Fig. 4(a)) and the contrast between maxima and minima we are able to deduce the orientation of the optical axis in the waveguide as well as the strength of birefringence. The underlying formula reads as

$$\frac{I_{transm}}{I_{total}} = \frac{1}{2}\sin^2\left[2\left(\alpha_{Pol} - \alpha_{wp}\right)\right]\left[1 - \cos(\Delta n k z)\right] \quad (9)$$

with I_{transm}/I_{total} as relative intensity transmission, α_{Pol} as orientation of the first polariser and α_{wp} as optical axis orientation of the evaluated wave plate, Δn as strength of the wave plate's birefringence, k as wave number and z as defect length. It can be seen that the transmitted intensity drops to zero for $\alpha_{Pol} = \alpha_{wp} + m \cdot 90^\circ$ ($m \in \mathbb{Z}$). Finding those points reveals the orientation of the wave plate's optical axis. In contrast, the maximum intensity transmission always occurs at 45° away from the minimum position. With the used wavelength and the thickness of the wave plate the strength of birefringence can be extracted.

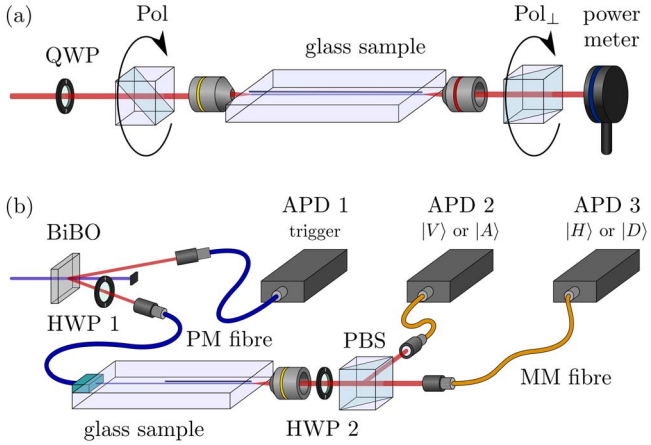

Figure 4 | Characterisation setups. (a) Classical characterisation of an arbitrary wave plate operation. The relative output of crossed polarisers gives information on the birefringence of the embedded waveguide. (b) Setting for the characterisation of the integrated quantum gates using single photons. One photon of a pair heralds the other one, which is in this case feed to the corresponding quantum gate via a butt-coupled fibre. The HWP 2 determines the measurement basis to be $|H\rangle$ and $|V\rangle$ or $|D\rangle$ and $|A\rangle$.

Quantum light measurement. We generate single photons at $\lambda = 815$ nm using a standard type I spontaneous parametric down-conversion source. A BiBO crystal is pumped by a 100 mW, 407.5 nm laser diode producing $|H\rangle$ polarised single photon pairs collected by polarisation maintaining (PM) fibres. Photon 1 is used to trigger the counts of the photon 2. This prevents the measurement from accidental counts caused by external photons or dark counts of the utilised avalanche photodiodes (APDs). By rotating half-wave plate (HWP) 1 photon 2 can be set to $|H\rangle$ or $|V\rangle$ before it passes the glass sample. The measurement basis can be aligned to $|H\rangle$ and $|V\rangle$ or $|D\rangle$ and $|A\rangle$ by rotating HWP 2 to 0° or 22.5°. Since a single photon state can be considered as a pure state, which means it is located on the surface of the Bloch sphere, the projections determined by HWP 2 yield in general two possible points $|\Psi\rangle_A$ and $|\Psi\rangle_B$ for the measured state. These points only differ in the complex phase distributed symmetrically around 0 or π, respectively. In other words $|\Psi\rangle_A$ and $|\Psi\rangle_B$ describe the same state irrespective if it is left or right circular. To get a knowledge about the sign of the complex phase and to have the ability to associate the output state to either $|\Psi\rangle_A$ or $|\Psi\rangle_B$, a qualitative examination using a quarter-wave plate is necessary, which was already done by the classical experiment.

The resulting state for a $|H\rangle$ and $|V\rangle$ input state is measured by collecting the outputs of a polarising beam splitter (PBS) for different bases via multi mode (MM) fibres. A sketch of the setting for the single photon characterization of the gates is shown in Fig. 4(b).

1. Nielsen, M. A. & Chuang, I. L. *Quantum Computation And Quantum Information* (Cambridge Univ. Press, 2000).
2. O'Brien, J. L., Furusawa, A. & Vukovic, J. Photonic quantum technologies. *Nature Photon.* **3**, 687–695 (2009).
3. Ladd, T. D. *et al.* Quantum computers. *Nature* **464**, 45–53 (2010).
4. Bloch, I. Quantum coherence and entanglement with ultracold atoms in optical lattices. *Nature* **453**, 1016–1022 (2008).
5. Kielpinski, D., Monroe, C. & Wineland, D. J. Architecture for a large-scale ion-trap quantum computer. *Nature* **417**, 709–711 (2002).
6. Blais, A., Huang, R.-S., Wallraff, A., Girvin, S. M. & Schoelkopf, R. J. Cavity quantum electrodynamics for superconducting electrical circuits: An architecture for quantum computation. *Phys. Rev. A* **69**, 062320 (2004).

7. Chiorescu, I., Nakamura, Y., Harmans, C. J. P. M. & Mooij, J. E. Coherent quantum dynamics of a superconducting flux qubit. *Science* **299**, 1869–1871 (2003).
8. Vandersypen, L. M. K. *et al*. Experimental realization of Shor's quantum factoring algorithm using nuclear magnetic resonance. *Nature* **414**, 883–887 (2001).
9. Politi, A., Cryan, M. J., Rarity, J. G., Yu, S. & O'Brien, J. L. Silica-on-silicon waveguide quantum circuits. *Science* **320**, 646–649 (2008).
10. Matthews, J. C. F., Politi, A., Stefanov, A. & O'Brien, J. L. Manipulation of multiphoton entanglement in waveguide quantum circuits. *Nature Photon.* **3**, 346–350 (2009).
11. Politi, A., Matthews, J. C. F. & O'Brien, J. L. Shor's quantum factoring algorithm on a photonic chip. *Science* **325**, 1221 (2009).
12. Peruzzo, A. *et al*. Quantum walks of correlated photons. *Science* **329**, 1500–1503 (2010).
13. Broome, M. A. *et al*. Photonic boson sampling in a tunable circuit. *Science* **339**, 794–798 (2013).
14. Tillmann, M. *et al*. Experimental boson sampling. *Nature Photon.* **7**, 540–544(2013).
15. Crespi, A. *et al*. Integrated multimode interferometers with arbitrary designs for photonic boson sampling. *Nature Photon.* **7**, 545–549 (2013).
16. Spring, J. B. *et al*. Boson sampling on a photonic chip. *Science* **339**, 798–801 (2013).
17. Mattle, K., Weinfurter, H., Kwiat, P. G. & Zeilinger, A. Dense coding in experimental quantum communication. *Phys. Rev. Lett.* **76**, 4656–4659 (1996).
18. Dousse, A. *et al*. Ultrabright source of entangled photon pairs. *Nature* **466**, 217–220 (2010).
19. Walther, P. *et al*. Experimental one-way quantum computing. *Nature* **434**, 169–176 (2005).
20. Ursin, R. *et al*. Entanglement-based quantum communication over 144 km. *Nature Phys.* **3**, 481–486 (2007).
21. Lanyon, B. P. *et al*. Towards quantum chemistry on a quantum computer. *Nature Chem.* **2**, 106 (2010).
22. Gündogan, M., Ledingham, P. M., Almasi, A., Cristiani, M. & de Riedmatten, H. Quantum storage of a photonic polarization qubit in a solid. *Phys. Rev. Lett.* **108**, 190504 (2012).
23. Thaniyavarn, S. Wavelength-independent, optical-damage-immune LiNbO3 TE? TM mode converter. *Opt. Lett.* **11**, 39–41 (1986)
24. Heismann, F. & Whalen, M. S. Broadband reset-free automatic polarization controller. *Electron. Lett.* **27**, 377–379 (1991).
25. Itoh, K., Watanabe, W., Nolte, S. & Schaffer, C. B. Ultrafast processes for bulk modification of transparent materials. *MRS Bulletin* **31**, 620–625 (2006).
26. Sansoni, L. *et al*. Polarization entangled state measurement on a chip. *Phys. Rev. Lett.* **105**, 200503 (2010).
27. Crespi, A. *et al*. Integrated photonic quantum gates for polarization qubits. *Nature Commun.* **2**, 566 (2011).
28. Crespi, A. *et al*. Anderson localization of entangled photons in an integrated quantum walk. *Nature Photon.* **7**, 322–328 (2013).
29. Di Giuseppe, G. *et al*. Einstein-Podolsky-Rosen spatial entanglement in ordered and Anderson photonic lattices. *Phys. Rev. Lett.* **110**, 150503 (2013)
30. Spagnolo, N. *et al*. Three-photon bosonic coalescence in an integrated tritter. *Nature Commun.* **4**, 1606 (2013).
31. Fernandes, L. A., Grenier, J. R., Herman, P. R., Aitchison, J. S. & Marques, P. V. S. Stress induced birefringence tuning in femtosecond laser fabricated waveguides in fused silica. *Opt. Express* **20**, 24103–24114 (2012).
32. Bhardwaj, V. *et al*. Stress in femtosecond-laser-written waveguides in fused silica. *Opt. Lett.* **29**, 1312–1314 (2004).
33. Yang, P., Burns, G. R., Guo, J., Luk, T. S. & Vawter, G. A. Femtosecond laser-pulse-induced birefringence in optically isotropic glass. *J. Appl. Phys.* **95**, 5280–5283 (2004).

Acknowledgments

The authors wish to thank the German Ministry of Education and Research (Center for Innovation Competence programme, grant 03Z1HN31), and the Thuringian Ministry for Education, Science and Culture (Research group Spacetime, grant no. 11027-514).

Author contributions

R.H. suggested the concept and did the theoretical analysis; R.H., M.G. and A.S. proposed the experimental realisation; R.H. and M.G. fabricated the samples and performed the measurements; R.H., M.G. and A.S. discussed the results; and R.H., M.G., S.N. and A.S. co-wrote the manuscript.

Additional information

Competing financial interests: The authors declare no competing financial interests.

How to cite this article: Heilmann, R., Gräfe, M., Nolte, S. & Szameit, A. Arbitrary photonic wave plate operations on chip: Realizing Hadamard, Pauli-X, and rotation gates for polarisation qubits. *Sci. Rep.* **4**, 4118; DOI:10.1038/srep04118 (2014).